Methylene Blue Photodegradation over STiM Composite

Maria Ulfa * and Amellia Ardhany

Chemistry Education Study Program, Faculty of Teacher Training and Education, Sebelas Maret University, Jl. Ir. Sutami 36A, Surakarta 57126, Indonesia
Email: ulfa.maria2015@gmail.com (M.U.); amelliaardhany12@student.uns.ac.id (A.A.)
*Corresponding author
Manuscript received November 1, 2025; revised January 5, 2026; accepted February 12, 2026; published July 22, 2026

Abstract*—This study reports the structural, optical, and photocatalytic characteristics of Si, Ti, and Silica-Titania-Manganese (STiM) nanocomposites synthesized under controlled conditions. X-Ray Diffraction (XRD) revealed distinct differences in crystallinity, with Si exhibiting the highest crystallinity (67.31%) and the smallest crystallite size (0.159 nm), Ti showing moderate crystallinity (56.3%, 0.223 nm), and STiM displaying the lowest crystallinity (42.2%) with the largest crystallite size (0.302 nm), indicating composite-induced disorder. Fourier-Transform Infrared (FTIR) spectra confirmed the presence of Si–O–Si vibrations in Si, Ti–O and Mn–O bonds in Ti, and combined features in STiM, suggesting strong interfacial interactions. Scanning Electron Microscopy (SEM) revealed particle sizes of 168 nm (Si), 932 nm (Ti), and 300 nm (STiM), while Energy-Dispersive X-ray (EDX) analysis confirmed the presence of TiO_2, SiO_2, and Mn dopants (0.37%) in the composite. Brunauer–Emmett–Teller (BET) analysis demonstrated significant differences in surface area, with Si exhibiting the highest SBET (763.2 m^2/g) and STiM showing hierarchical microporous–mesoporous structures. UV-Vis Diffuse Reflectance Spectroscopy (UV-DRS) revealed bandgap narrowing in STiM (indirect Eg = 1.08 eV), enhancing visible-light absorption. Photocatalytic tests against methylene blue showed superior performance of STiM (77.4%) compared to Ti (27.4%) and Si (7.4%), with adsorption kinetics best described by the pseudo-second-order model. These results highlight the synergistic role of Si–Ti interactions and Mn doping in optimizing photocatalytic activity.

***Keywords*—Si-Ti-Mn, nanocomposites, visible-light photocatalysis, methylene blue degradation, pseudo-second-order kinetics, bandgap narrowing**

I. Introduction

The continuous discharge of synthetic dye-laden effluents from textile, leather, and printing industries poses a serious threat to water quality, directly challenging the implementation of Sustainable Development Goal (SDG) 6 (Clean Water and Sanitation). This issue is further aligned with SDG 12, which promotes sustainable industrial wastewater management, and SDG 14, as dye pollution adversely affects aquatic life and ecosystem integrity [1]. Among these dyes, Methylene Blue (MB) is one of the most widely used cationic dyes, exhibiting strong chemical stability, resistance to biodegradation, and potential toxicity to aquatic ecosystems and human health [2]. Conventional treatment methods such as adsorption, coagulation, and biological degradation are often inadequate for complete mineralization of MB, thereby motivating the exploration of Advanced Oxidation Processes (AOPs), particularly semiconductor-based photocatalysis, as an efficient and sustainable remediation strategy [3, 4]. Thin-film photocatalysts offer superior mechanical stability, reusability, and compatibility with fixed-bed and device-integrated systems compared to nanoparticle suspensions, which often suffer from aggregation and recovery challenges. However, their relatively lower surface area necessitates structural and electronic optimization.

II. Literature Review

Titanium dioxide (TiO_2) has long been recognized as a benchmark photocatalyst due to its strong oxidizing ability, chemical stability, and nontoxicity [5]. However, its relatively wide band gap (~3.2 eV) restricts its photoactivity primarily to the UV region, which constitutes only a small fraction of solar irradiation [6]. To overcome this limitation, various modification strategies have been employed, including metal and non-metal doping, heterojunction engineering, and the incorporation of transition metal oxides. Manganese-based materials, in particular, have attracted increasing attention owing to their multiple oxidation states, high redox flexibility, and ability to promote charge carrier separation while extending light absorption into the visible spectrum [7, 8].

The use of silica as a hard template offers additional benefits in photocatalyst design [9]. Silica possesses a high surface area, a tunable pore structure, and excellent stability, which can serve as a robust support to disperse active photocatalytic species [10]. Moreover, silica-assisted templating helps control the particle size and prevents agglomeration of TiO_2 and transition metal oxides, thereby enhancing the accessibility of active sites during photocatalytic reactions [11]. By integrating silica with titania and manganese, a ternary composite—hereafter referred to as Silica-Titania-Manganese (STiM)—can be engineered to exploit the synergistic effects among the three components: Improved charge separation, enhanced light harvesting, and surface-driven catalytic activity.

Although several studies have reported the advantages of TiO_2–MnO_x systems or silica-based photocatalysts individually, systematic investigations that directly compare the catalytic efficiency of STiM composites with hard-template silica and pure TiO_2 remain limited. Such comparative studies are crucial to elucidate the distinct role of each component in enhancing photocatalytic performance, particularly for dye degradation applications.

Therefore, this study aims to investigate the photocatalytic degradation of methylene blue using an STiM composite in comparison with hard-template silica and pure TiO_2. The catalytic performance is systematically evaluated in terms of degradation efficiency and kinetic behavior, with emphasis on understanding the structural, morphological, and electronic properties underlying the observed activity. This work is expected to provide deeper insight into the rational

design of ternary oxide–silica composites for efficient solar-driven wastewater treatment.

III. Material and Methods

A. Materials and Chemicals

Tetraethyl orthosilicate (TEOS, $Si(OC_2H_5)_4$, ≥98%, Sigma-Aldrich, MW = 208.33 g·mol^{-1}) was employed as the silica precursor, titanium(IV) ethoxide ($Ti(OC_2H_5)_4$, 99%, Sigma-Aldrich, MW = 228.15 g·mol^{-1}) as the titania source, and manganese(IV) oxide (MnO_2, 99%, Merck, MW = 86.94 g·mol^{-1}) as the manganese precursor. Pluronic P123 (EO_{20}–PO_{70}–EO_{20}, Sigma-Aldrich) served as the structure-directing agent, hydrochloric acid (HCl, 37%, Merck) was used as the hydrolysis catalyst, and sodium hydroxide pellets (≥98%, Merck) were applied for selective silica removal. Ethanol (≥99.8%, Merck, MW = 46.07 g·mol^{-1}) acted as solvent, while methylene blue ($C_{16}H_{18}ClN_3S \cdot xH_2O$, analytical grade, Merck, MW = 319.85 g·mol^{-1}) was employed as the model dye pollutant. Deionized water (18.2 MΩ·cm) was used throughout all synthetic and photocatalytic experiments.

B. Synthesis of Hard-Template Silica (S)

Mesoporous silica hard template (denoted as S) was prepared by dissolving Pluronic P123 in 1.6 M HCl at 35 °C, followed by dropwise addition of TEOS with a molar ratio of $Si(OC_2H_5)_4$:P123:HCl:H_2O = 1:0.017:6:200. The mixture was stirred for 24 h at 35 °C and subsequently subjected to hydrothermal treatment at 100 °C for 24 h. The resulting solid was filtered, washed thoroughly with deionized water, dried at 60 °C overnight, and finally calcined at 550 °C for 5 h to remove organic moieties, yielding the mesoporous silica template.

C. Synthesis of Pure TiO_2

Pure titania (Ti) was synthesized by dissolving titanium(IV) ethoxide in ethanol, followed by controlled hydrolysis with deionized water at a molar ratio of $Ti(OC_2H_5)_4$:H_2O:EtOH = 1:10:20. The suspension was stirred at ambient temperature for 12 h, dried at 80 °C, and calcined at 500 °C for 4 h to obtain crystalline TiO_2 powder.

D. Synthesis of Silica-Titania-Manganese Composite (STiM)

The Silica-Titania-Manganese (STiM) composite was synthesized via a hard-template strategy employing preformed silica (S) as the structural framework. One gram of silica S was dispersed in ethanol and ultrasonicated to obtain a homogeneous suspension. A precursor solution containing titanium(IV) ethoxide and manganese(IV) oxide was prepared in ethanol at a Ti:Mn molar ratio of 9:1, followed by gradual addition into the silica suspension under vigorous stirring. The mixture was aged for 24 h at room temperature to ensure uniform incorporation of the metal species. The resulting slurry was dried at 80 °C and subsequently calcined at 500 °C for 5 h. To develop the mesoporous architecture, the silica template was selectively removed by alkaline leaching in 2 M NaOH at 90 °C for 10 h. The obtained solid was thoroughly washed with deionized water until neutral pH, dried at 60 °C, and designated as STiM.

E. Characterization Techniques

The crystalline phases of the materials were identified by X-Ray Diffraction (XRD, Panalytical PW 3050/60, Cu Kα radiation, λ = 1.5406 Å). Functional groups were analyzed by Fourier-Transform Infrared spectroscopy (FTIR, Shimadzu IR-Prestige-21). Morphological and elemental features were examined using scanning electron microscopy coupled with energy-dispersive X-ray spectroscopy (Scanning Electron Microscopy (SEM)-Energy-Dispersive X-ray (EDX), JEOL JSM-700, 15.0 kV). Optical properties and band gap energies were determined via UV–Vis diffuse reflectance spectroscopy (UV-Vis Diffuse Reflectance Spectroscopy (DRS), Analytik Jena Specord 200 Plus). Surface area, pore volume, and pore size distribution were evaluated by nitrogen adsorption–desorption analysis employing the Brunauer–Emmett–Teller (BET) method (Micromeritics ASAP 2020).

F. Photocatalytic Activity Test

Photocatalytic activity was assessed through the degradation of blue. Typically, 50 mg of photocatalyst (S, Ti, or STiM) was dispersed in 200 mL of MB solution (20 mg·L^{-1}). The suspension was magnetically stirred in the dark for 30 min to achieve adsorption-desorption equilibrium, followed by visible-light irradiation. At predetermined intervals, aliquots were withdrawn, centrifuged to separate solid catalysts, and analyzed by UV–Vis spectrophotometry (Shimadzu UV-3600) at the maximum absorption wavelength of 664 nm. The degradation efficiency was calculated from the relative concentration decrease of MB with respect to the initial state. Photocatalytic experiments were conducted under visible-light irradiation (λ > 420 nm) with a measured photon flux of 10 mW cm^{-2}.

IV. Result and Discussion

A. XRD

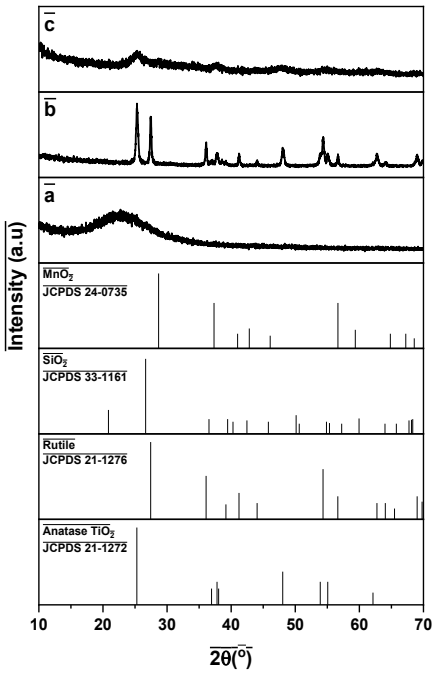

Fig. 1. XRD difftactogram: (a) Hard-Template Silica (Si), (b) pure TiO_2 and (c) STiM.

The XRD diffractograms (Fig. 1) show significant differences in structural characteristics between the three samples analyzed. Sample (a) shows a diffraction pattern dominated by broad humps characteristic of amorphous materials with low intensity, indicating a disordered structure or very low crystallinity [12]. Sample (b) displays sharp and well-defined diffraction peaks, indicating high crystallinity with a dominant anatase TiO_2 phase based on the characteristic peak at $2\theta \approx 25°$ and other secondary peaks in accordance with JCPDS 21-1272 [13]. Sample (c) shows a diffraction pattern very similar to sample (a), with broad humps indicating an amorphous structure [14]. Comparison with JCPDS reference data shows that the samples contain a mixture of MnO_2 (JCPDS 24-0735), amorphous SiO_2 (JCPDS 33-1161), rutile TiO_2 (JCPDS 21-1276), and anatase TiO_2 (JCPDS 21-1272) phases, where the dominance of a particular phase varies between samples [15, 16].

Differences in diffraction patterns indicate variations in synthesis conditions or thermal treatments that affect the degree of crystallinity and phase composition. A recent study by Putri *et al*. [17] showed that calcination temperature has a significant influence on phase transformation, where increasing temperature can cause a transition from anatase to rutile phase in TiO_2 and the formation of a more ordered crystal structure. Duarte *et al.* [18] confirmed that materials with high crystallinity (such as sample (b)) exhibit superior photocatalytic activity compared to amorphous structures due to fewer crystal defects and better charge carrier mobility. The presence of an amorphous phase in samples (a) and (c) can be attributed to the synthesis conditions that produce materials with irregular structures, which potentially have high specific surface areas but have limited catalytic activity. Kim *et al*. [19] showed that precise control of synthesis parameters can optimize the crystalline phase ratio to maximize performance for specific applications.

Table 1. Diameter crystal and crystallinity

Sample	D (nm)	Crystallinity (%)	Quantitative comparison with literature	Ref.
Si	0.159	67.305	SiO_2-based porous materials reported for photocatalytic applications generally exhibit moderate to high crystallinity depending on morphology and synthesis conditions	[13]
Ti	0.223	56.344	Titania synthesized using soft templates such as Pluronic P123 and gelatin shows crystallinity values in a comparable range, influenced by organic template ratio	[14]
STiM	0.302	42.162	This work	-

XRD data shows a clear trend that the crystallite size (D) is inversely proportional to the percentage of crystallinity of the samples (Table 1) The Si sample with the smallest crystallite size (0.159 nm) shows the highest crystallinity (67.305%), followed by Ti (0.223 nm; 56.344%), and STIM with the largest crystallite size (0.302 nm) shows the lowest crystallinity (42.162%). This relationship is consistent with the theory of X-ray diffraction which states that materials with nano-sized crystals tend to have a more regular structure and higher crystallinity. According to a recent study by Nasiri *et al*. [20], the crystallite size calculated using the Scherrer equation has a direct correlation with the degree of regularity of the crystal structure of nanocrystalline materials. Ilmi *et al.* [21] also confirmed that materials with smaller crystallite sizes generally exhibit sharper diffraction peaks and higher intensities, indicating superior crystallinity.

STiM samples exhibit interesting characteristics with the largest crystallite size but the lowest crystallinity. This phenomenon can be explained by the formation of a complex composite structure where the interaction between Si and Ti results in larger crystal domains but with a reduced degree of order. Teamsinsungvon *et al.* [22] showed that composite formation can result in particle agglomeration that affects the crystallite size distribution and overall crystallinity. Nandanwar *et al.* [23] study on TiO_2/SiO_2 nanocomposites also confirmed that the addition of silica can slow down the growth of TiO_2 crystals, but can reduce the overall crystallinity due to the formation of an amorphous phase at the interface. These results indicate that despite the increase in crystallite size, the phase distribution and structural order in STiM composites decrease.

The differences in crystallite size and crystallinity of the three samples have significant implications for their physicochemical properties and potential applications. Si samples with high crystallinity and small crystallite size have the potential to exhibit superior catalytic activity and specific surface area, as confirmed by the study of Diputra et al. which showed a correlation between nanocrystallite size and increased material activity [24]. Meanwhile, STiM samples with larger crystallite size can exhibit better thermal stability but with limited surface activity. According to the study of Ulhakim *et al.* [25] on TiO_2, materials with crystallite sizes in the range of 16–30 nm exhibit an optimal balance between stability and reactivity. These XRD data indicate that optimization of synthesis parameters for STiM samples is necessary to achieve a balance between crystallite size and crystallinity to maximize material performance for specific applications such as photocatalysis or sensors.

B. FTIR

The FTIR spectra show significant characteristic differences between the three samples (a, b, and c), indicating variations in the composition and chemical structure of the materials. Sample (a) displays typical absorption for silica-based materials with a broad peak in the region of 3000–3500 cm^{-1} which is the stretching vibration of the O–H groups of adsorbed water molecules and silanol (Si–OH) groups on the surface of silica particles [26]. The characteristic peak at around 1000–1100 cm^{-1} indicates the asymmetric stretching vibration of the Si–O–Si bond which is characteristic of the amorphous silica structure [27]. Sample (b) shows a relatively flat transmittance intensity with several sharp peaks in the region of 500–800 cm^{-1}, indicating the presence of crystalline metal oxides with characteristic vibrations of Ti–O and Mn–O [28, 29]. Sample (c) shows a combination of the characteristics of the previous two samples with a broad peak in the region of 3000–4000 cm^{-1} and complex absorption in the fingerprint region [30].

The absorption peaks in the 3000–3500 cm^{-1} region in samples (a) and (c) indicate the presence of hydrogen-bonded hydroxyl groups with a frequency shift towards lower

wavenumbers, indicating the formation of strong hydrogen bonds [31]. Recent research by Ellerbrock *et al.* [27] confirmed that the peak at 3700–3600 cm^{-1} represents free O–H vibrations without hydrogen bonds, while the shift to lower frequencies (3000–3500 cm^{-1}) indicates the formation of hydrogenated structures. For the metal oxide material in sample (b), the absorption at 500–700 cm^{-1} can be attributed to the Ti–O stretching vibrations in anatase and rutile TiO_2 (around 500–600 cm^{-1}) and Mn–O vibrations in MnO_2 (around 500–630 cm^{-1}). The study of Mousa *et al*. [32] showed that the TiO_2/MnO_2 composite displayed characteristic peaks of Ti–O at 627 cm^{-1} and Mn-O in the range of 500–635 cm^{-1}.

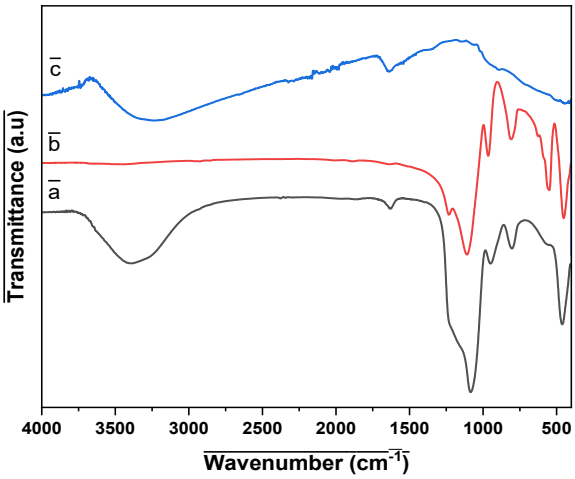

Fig. 2. FTIR spectra a. hard-template silica (Si), b. pure TiO_2 and c. STiM.

The differences in the FTIR spectral profiles (Fig. 2) indicate that sample (a) is a silica-based material with a high degree of hydration, sample (b) is a crystalline metal oxide with a more ordered structure, and sample (c) is a composite material that combines the characteristics of both components. Ramaripa *et al*. [28] showed that the formation of TiO_2-MOF composites resulted in shifts and changes in the FTIR peak intensity, indicating chemical interactions between the components. The presence of a broad peak at 1000–1100 cm^{-1} in samples (a) and (c) indicates a Si-O-Si structure that can act as a supporting matrix for metal oxide particles, as confirmed by the study of Budiarti *et al.* [33] on the core-shell $SiO_2@TiO_2$ system. These spectral characteristics indicate that the composite material (sample (c)) has superior application potential in the fields of catalysis and adsorption because it combines the high surface area of the silica component with the catalytic activity of the metal oxide [33].

C. SEM

SEM data showed significant particle diameter variations between Si, Ti, and STIM samples with values of 0.168 µm, 0.932 µm, and 0.300 µm, respectively (Fig. 3). The Si sample exhibited the smallest diameter in the sub-micron range (168 nm), indicating the formation of uniform nano-submicron particles. Recent research by Wei *et al.* [34] confirmed that SEM analysis can identify particle size variations with high accuracy, with smaller particles generally exhibiting a more homogeneous distribution and a more regular morphology. The Ti sample exhibited the largest diameter (932 nm), nearly approaching 1 µm, indicating particle growth or agglomeration during the synthesis process. Bals and Epple [35] showed that titanium particles tend to agglomerate due to their high surface energy, resulting in structures with sizes larger than their individual components. The STiM composite sample with a diameter of 300 nm exhibited intermediate characteristics, indicating the formation of a composite structure that successfully controlled particle growth through interactions between components.

Variations in particle diameter (Table 2) reflect differences in nucleation and growth during synthesis. The small Si particles (~168 nm) indicate synthesis conditions favoring homogeneous nucleation and controlled growth, likely via precipitation or sol–gel routes, resulting in a narrow size distribution. This behavior is consistent with reported Ti–Si composites synthesized under controlled conditions, which exhibit uniform particle sizes and good spherical morphology [36]. The Ti sample, exhibiting the largest particle diameter (~932 nm), suggests secondary agglomeration or Ostwald ripening, where smaller particles dissolve and redeposit onto larger ones. Such growth behavior is known to be governed by synthesis parameters including temperature, pH, and precursor concentration, as reported in related studies [36–38]. The STiM sample highlights the ability of composite systems to regulate particle size through synergistic Si–Ti interactions, where one component acts as a stabilizing or templating agent, limiting particle growth and yielding sizes suitable for targeted applications.

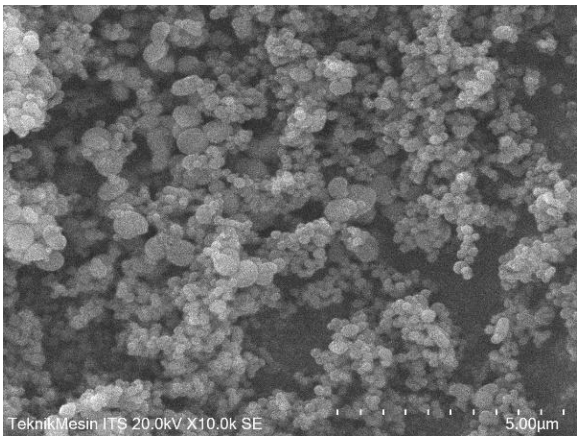

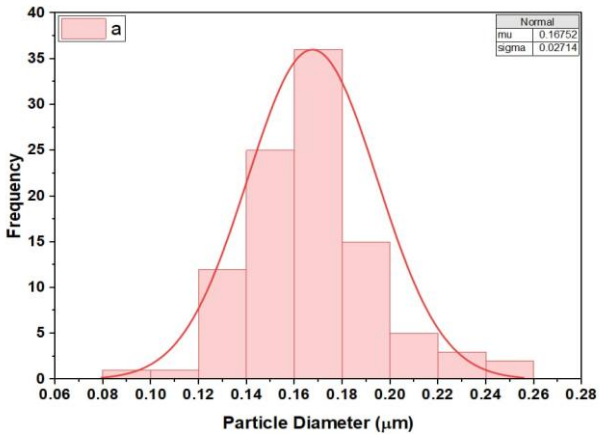

(a)

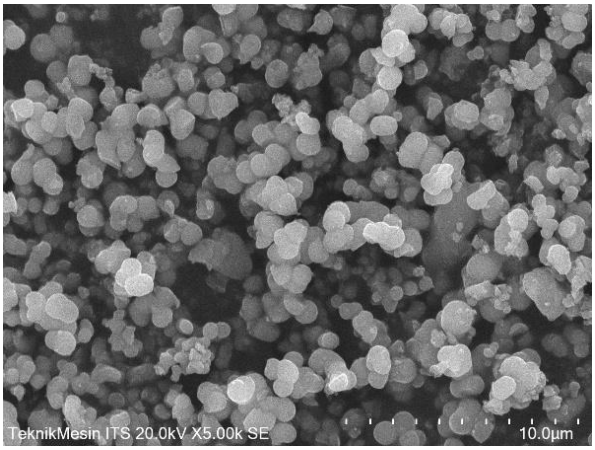

(a)

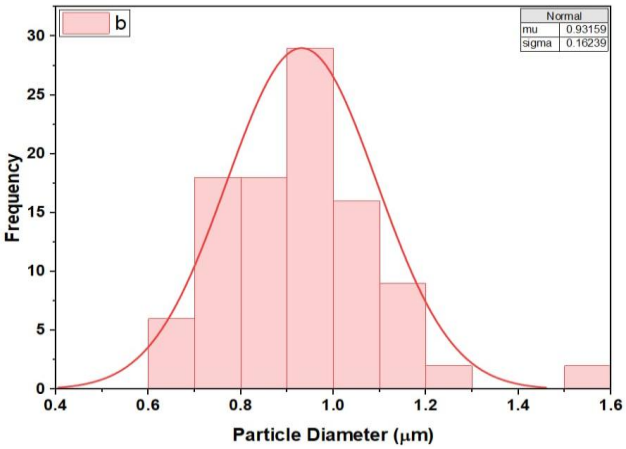

(b)

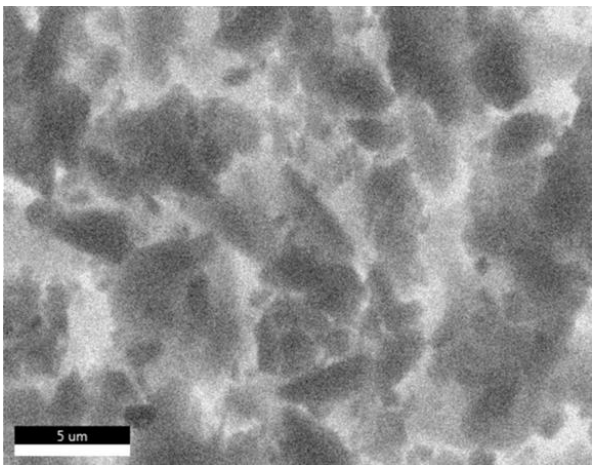

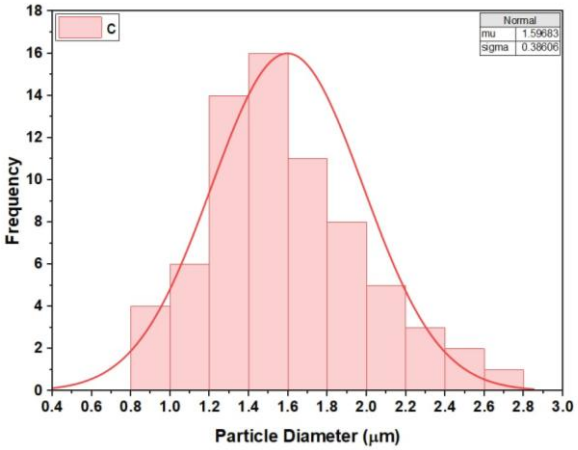

(c)

Fig. 3. SEM. (a). Hard-template silica (Si), (b). pure TiO_2, (c). STiM.

Table 2. Particle diameter

Sample	Diameter (µm)
Si	0.168
Ti	0.932
STiM	0.300

D. EDX

EDX analysis of the STiM sample identified five main elements with mass fractions of O (72.51%), Ti (20.83%), Na (4.27%), Si (2.01%), and Mn (0.37%) (Table 3). The high oxygen content confirms an oxide-dominated matrix, consistent with TiO_2 as the primary photocatalytic phase. The substantial Ti fraction further supports the dominance of TiO_2, while the low Si content suggests the presence of a thin SiO_2 layer or surface doping, in agreement with reported TiO_2@SiO_2 composites showing SiO_2 contents in the range of 0.79–3.12%. The detected Na is attributed to residual Na_2SiO_3 used as the silica precursor during synthesis [39].

Table 3. EDX result of all sample

Sample	Weight (%)				
	O	Na	Si	Ti	Mn
STiM	72.51	4.27	2.01	20.83	0.37
Silica	56.73	-	43.27	-	-
MnO_2	50.44	-	-	-	49.56
TiO_2	32.98	-	-	67.02	-

The manganese content of 0.37%, although low, indicates the presence of Mn doping in the composite structure, which has the potential to modify electronic properties and enhance photocatalytic activity through the formation of new energy levels and electron capture centers. Research by Mousa *et al.* [32] on TiO_2/MnO_2 nanocomposites showed that Mn dopants, even in small amounts (0.5–2%), can lower the band gap energy and enhance charge transfer, thereby accelerating the degradation of organic pollutants. The appropriate Mn value in the STiM sample (0.37%) indicates optimization of the dopant dosage to balance reducing electron-hole recombination and maintaining the crystal structure of TiO_2.

The elemental mapping analysis in the study by Kadri *et al.* [40] showed a homogeneous distribution of Ti, Si, and O on the surface of TiO_2–SiO_2 nanofilms, without local accumulation of other precursor elements. Although the STiM sample does not show an elemental map here, the EDX composition is relatively consistent with the literature values indicating compositional homogeneity. The successful deposition of SiO_2 and doping of Mn and residual Na is reflected in the elemental mass distribution, confirming that the synthesis method used produces nanocomposites with a uniform elemental distribution and composition according to the photocatalyst material design.

E. BET

The isotherms (Fig. 4) displayed by samples a and b belong to Type IV with clear hysteresis loops at relative pressures (P/P_0) between 0.4 and 0.9, indicating a mesoporous structure [41]. Sample (a) exhibits a maximum adsorption volume of ~450 cc/g, indicating a very large surface area and pore volume of mesoporous material due to the connected porous structure; its hysteresis loop tends to be H1-shaped,

indicating regular cylindrical pores with a narrow size distribution [42]. In contrast, sample (b) has a maximum adsorption capacity of ~140 cc/g and an H3-shaped hysteresis loop, indicating plate-shaped or slit-like pores that are less regular and imperfectly connected. In both samples, there is a volume difference between the adsorption and desorption paths, reflecting the effect of capillary condensation and the retention of N_2 molecules within the mesopores.

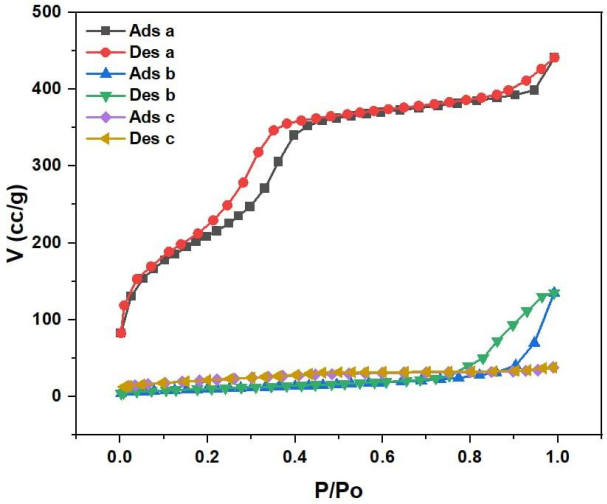

Fig. 4. Isotherm BET. a. Hard-Template Silica (Si), b. pure TiO_2 and c. STiM.

Sample (c) exhibits an isotherm close to Type II with a very narrow hysteresis loop (~30 cc/g), indicating a predominantly nonporous or microporous structure with minimal mesopore contribution. The nearly linear adsorption behavior at $P/P_0 < 0.1$ suggests monolayer–multilayer formation on the external surface, while the negligible hysteresis at $P/P_0 > 0.4$ confirms the absence of interconnected pores required for capillary condensation [43]. Sample (c) exhibits an isotherm close to Type II with a very narrow hysteresis loop (~30 cc/g), indicating a predominantly nonporous or microporous structure with minimal mesopore contribution. The nearly linear adsorption behavior at $P/P_0 < 0.1$ suggests monolayer-multilayer formation on the external surface, while the negligible hysteresis at $P/P_0 > 0.4$ confirms the absence of interconnected pores required for capillary condensation.

Sample (a) shows the highest pore volume distribution (Fig. 5) at a radius of approximately 15–20 Å, with a dramatic peak that decreases sharply with increasing radius, indicating the dominance of small to medium-sized mesoporous pores (1.5–2.0 nm). This curve shape is consistent with a material with a narrow connected pore network, as reported by Bonne *et al*. [44] in TiO_2-SiO_2 nanocomposites that displayed a pore volume peak centered at a radius of ~20 Å due to the regular mesoporous structure. The steep curve after the peak indicates the presence of strong condensation capillaries in the narrow pores, supporting the Type IV isotherm results that show H1 hysteresis in sample (a).

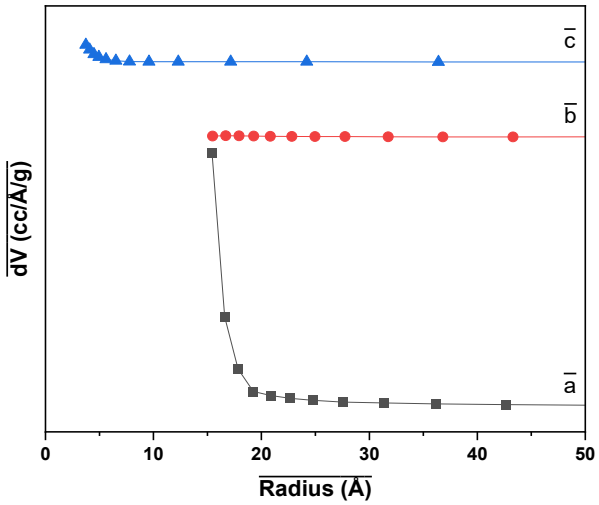

Fig. 5. Radius pore: (a) Hard-Template Silica (Si), (b) pure TiO_2 and (c) STiM.

By comparison samples (b) and (c) exhibit nearly flat pore volume distributions, indicating a negligible contribution from pores of specific sizes. Sample (b) shows a slight increase in dv at radii above 40 Å, suggesting the presence of large pores, consistent with the H3 hysteresis observed in the BET isotherm. Meanwhile, sample (c) shows almost no variation in dv, indicating a nonporous structure or the dominance of very large pores outside the measurable range (0–50 Å). This behavior is consistent with compact materials lacking a well-defined pore structure, as previously reported in the literature [43].

Table 4. BET of all samples

Samples	S_{BET} (m^2/g)	S_{micro} [a] (m^2/g)	S_{meso} [b] (m^2/g)	V_{micro} [a] (cc/g)	V_{meso} [b] (cc/g)	V_{total} (cc/g)	D^b (nm)
Si	763.226	0.000	282.300	0.000	0.3389	0.3389	1.542
Ti	37.928	0.000	31.060	0.000	0.2045	0.2045	1.670
STiM	76.619	20.701	8.773	0.00974	0.0195	0.02924	3.742

[a] S_{micro} and V_{micro} determined by t-plot method
[b] S_{meso}, V_{meso}, and pore diameter (D) determined by BJH method

The BET analysis results showed significant variations in specific surface area (SBET) between the three samples, with the Si sample having the highest value (763.226 m^2/g), followed by Ti (37.928 m^2/g), and STiM the lowest (76.619 m^2/g). The t-plot data revealed that the Si and Ti samples did not show microporosity (Smicro = 0.000 m^2/g), while the STIiM sample had a microporous surface area of 20.701 m^2/g with a micropore volume of 0.00974 cc/g (Table 4). The BJH analysis showed that the Si sample had the highest mesoporous surface area (282.300 m^2/g) and the largest mesoporous volume (0.3389 cc/g), while STiM showed much lower values (8.773 m^2/g for Smeso and 0.0195 cc/g for Vmeso). Recent research by Garvie confirmed that the t-plot method provides accurate information on the distribution of micropores and mesoporosity, where the presence of microporosity indicates the formation of a more complex structure in the composite material [43]. The study of Teamsinsungvon *et al*. [22] on the TixSiy system showed that Ti-Si composites with an optimal ratio can produce a surface area of up to 225.68 m^2/g with a diverse pore distribution.

Pore diameter data shows that the STiM sample has the

largest pore diameter (3.742 nm), followed by Ti (1.670 nm) and Si (1.542 nm), indicating the formation of different pore structures due to the material composition. The presence of microporosity in STiM (20.701 m^2/g) indicates the formation of a hierarchical structure combining micropores and mesopores, as confirmed by the study of Xiao *et al.* [45] which showed that SiO_2 coating on TiO_2 can produce materials with a surface area of up to 160.52 m^2/g and pore diameters in the range of 4–5 nm [44]. The significant difference in total pore volume (Vtotal) where Si shows the highest value (0.3389 cc/g) compared to STiM (0.02924 cc/g) indicates that the formation of the composite fundamentally changes the pore structure. The study of Bonne *et al.* [44] on TiO_2-SiO_2 nanocomposites showed that the material with a high surface area can maintain its structure even with titania loading up to 55 wt%. These results indicate that the STiM sample successfully formed a unique composite structure with a combination of micropores and mesopores, which has the potential to provide advantages in catalysis and adsorption applications because it provides diverse diffusion pathways for molecules with different sizes [46]. Pore structure analysis in this study was based on BET surface area measurements and BJH pore size distribution. While these methods provide qualitative insight into mesoporous characteristics, more advanced pore modeling, such as NLDFT, was not conducted due to limited access to the required analytical facilities. Future work will incorporate NLDFT-based pore size distribution analysis to achieve a more accurate and quantitative description of pore geometry and connectivity, particularly for complex mesoporous photocatalytic systems.

F. UV-DRS

UV-DRS data showed significant differences in the bandgap energy values between the direct and indirect transitions for Ti and STiM samples. The Ti sample exhibited a direct bandgap energy of 2.814 eV and an indirect one of 2.732 eV, with a relatively small difference of 0.082 eV, indicating the characteristics of a semiconductor with a nearly direct transition. A recent study by Makuła *et al.* [46] confirmed that anatase TiO_2 exhibits a dominant indirect transition with a bandgap value of about 3.2 eV; however, lower values, such as those obtained, could be attributed to structural modifications or defects in the crystal lattice. The STiM sample showed a different pattern with a direct bandgap energy of 2.906 eV and an indirect one of 1.077 eV, where the very large difference (1.829 eV) indicates a fundamental change in the electronic structure of the material. Landi *et al.* [47] showed that TiO_2 particles synthesized via precipitation can exhibit significant variations in bandgap values depending on the synthesis conditions and particle size.

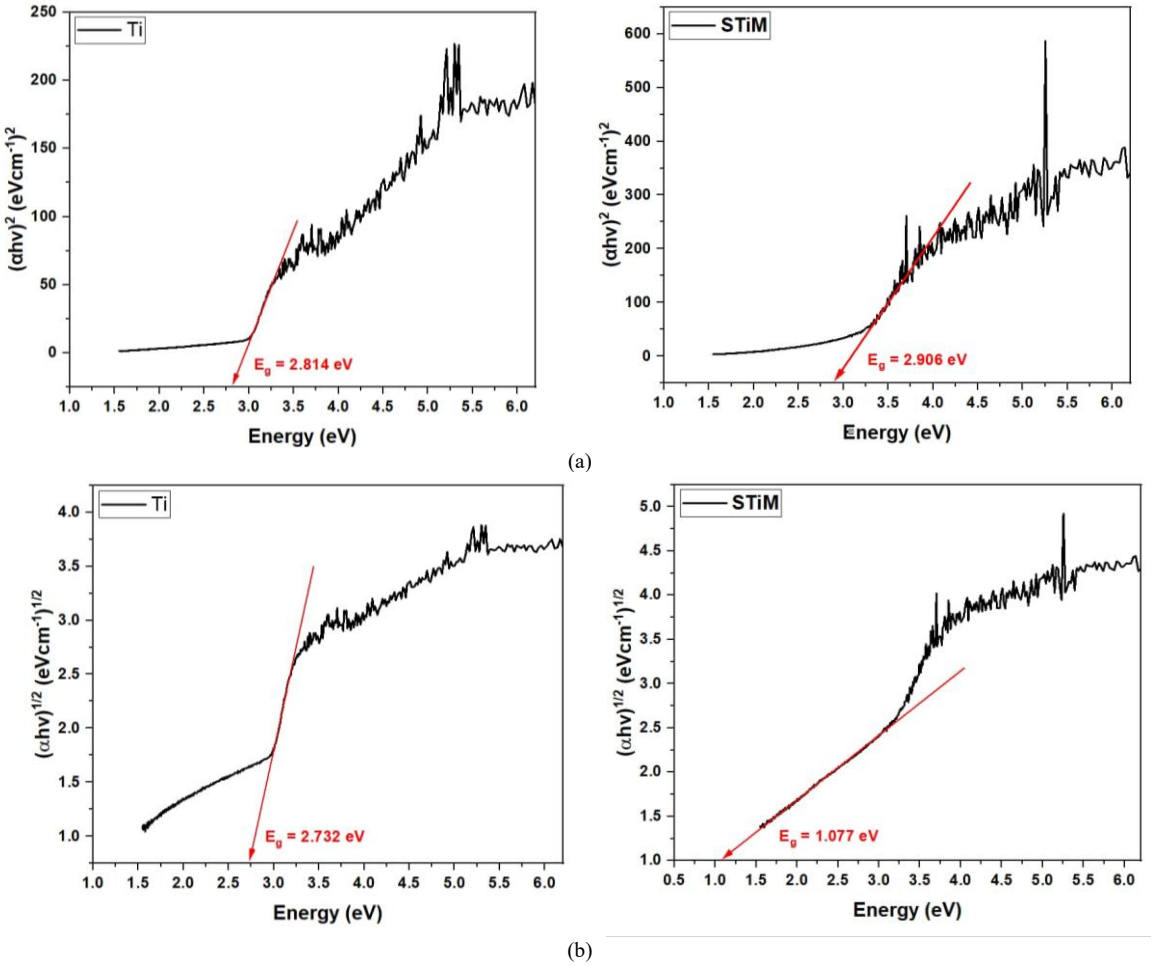

Fig. 6. UV-DRS spectra of (a). direct and (b). indirect mode.

The STiM sample shows an interesting phenomenon where the indirect transition has a much lower bandgap value (1.077 eV) compared to the direct transition (2.906 eV), indicating the formation of a composite structure that

successfully changes the electronic characteristics of the material (Fig. 6). Research on TiO_2/SiO_2 from MCM-41 composites shows a decrease in the bandgap from 3.2 eV to 2.9 eV, which is associated with the formation of new energy levels due to interactions between components [29]. The very low indirect bandgap value in STiM (1.077 eV) indicates success in bandgap engineering, where the composite material successfully creates an easier electronic transition path through the indirect transition mechanism (Table 5). A study by Halder *et al.* [48] confirmed that the transition from direct to indirect bandgap in composite materials can significantly affect the photocatalytic efficiency of the material. Hariani *et al.* [49] also showed a decrease in the bandgap from 3.24 eV to 2.92 eV, confirming that the formation of the composite can effectively modify the optical properties of the material.

Table 5. Band gap energy

Sample	Bandgap Energy (eV)	
	Direct $((\alpha hv)^2$ $(eVcm^{-1})^2)$	Indirect $((ahv)^{1/2}$ $(eVcm^{-1})^{1/2})$
Ti	2.814	2.732
STiM	2.906	1.077

The significant difference in bandgap values between Ti and STiM samples has important implications for the practical applications of these materials. Ti samples with a bandgap in the range of 2.7–2.8 eV show good visible light absorption capabilities, but are still limited to the high-energy region. STiM samples with an indirect bandgap of 1.077 eV show remarkable potential for photocatalytic applications in the visible to near-infrared spectrum, as confirmed by the study of Tasisa *et al*. [50], who showed that TiO_2 materials with a narrowed bandgap can significantly enhance solar light absorption. Doyan *et al.* [51] confirmed that reducing the bandgap in metal oxide-based materials can improve solar energy conversion efficiency. The low bandgap value of the indirect transition of STiM indicates the formation of an optimal electronic structure for applications in solar cells and photocatalysis, where the material can utilize a wider light spectrum. However, the large difference between the direct and indirect transitions also indicates the complexity of the electronic structure that requires further characterization to understand the charge carrier transport mechanism and the efficiency of electron-hole recombination in practical applications.

G. Photocatalytic

The data showed significant differences in removal efficiency between the three samples, with the STiM sample showing the highest performance with an efficiency of 77.381%, followed by Ti (27.381%) and Si (7.381%). The experimental adsorption capacity (q_e Exp) values also showed a consistent trend with removal efficiency, with STiM having the highest q_e (0.001845 mg/g), Ti (0.000597 mg/g), and Si the lowest (0.000197 mg/g) (Fig. 7). Khaliha *et al.* [52] emphasized that comparisons of removal efficiency should consider different experimental conditions, and composite materials generally showed superior performance compared to their single components. The study by Hadian *et al.* [53] on $TiO_2/ZnO/SiO_2$ composites confirmed that composite formation can significantly improve removal efficiency to higher values than the individual materials. These results indicate that the formation of the STiM composite structure successfully optimizes the adsorbate-adsorbent interaction through synergism between the Si and Ti components.

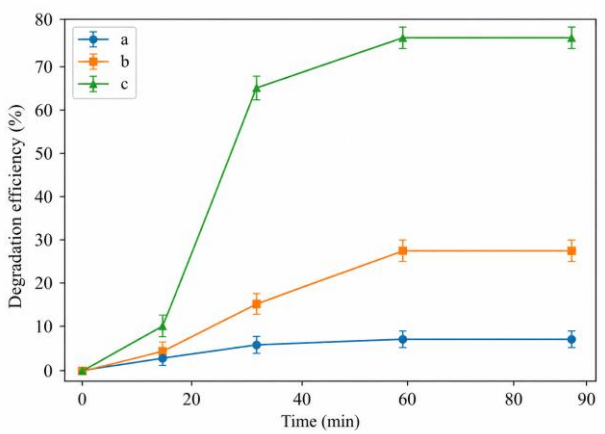

Fig. 7. Photodegradation of Methylene Blue using a. Silica only, b. Titania only c. STiM.

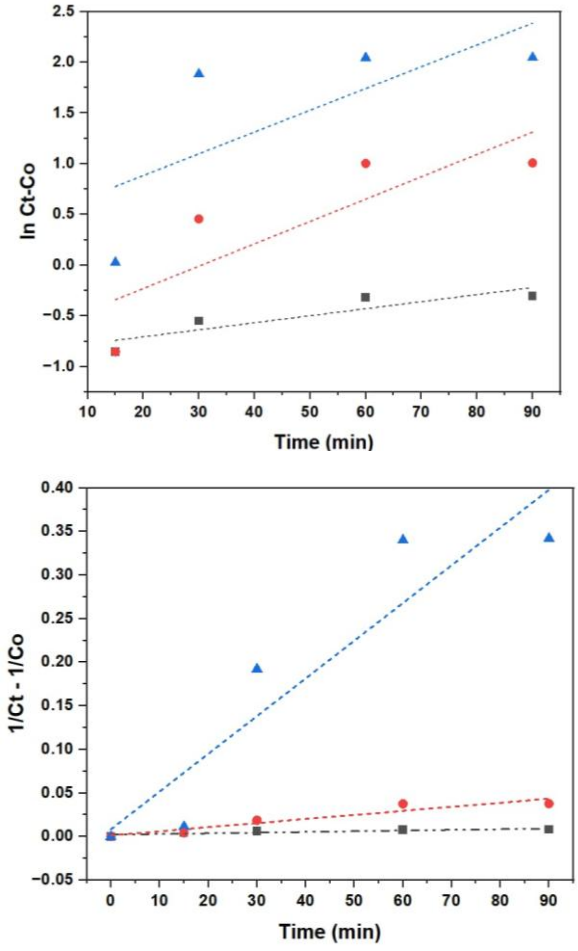

Fig. 8. Figure Kinetic model of a. Si (blue triangle), b. Ti (red dot) and c. STiM (black square) by Pseudo first (top) and second (bottom) order.

Kinetic model evaluation showed that all samples followed a pseudo-second-order model with a higher correlation coefficient (R^2) than the pseudo-first-order model. The Ti sample showed the best fit for the pseudo-second-order model ($R^2 = 0.86629$), followed by STIM ($R^2 = 0.82158$) and Si ($R^2 = 0.65961$) (Fig. 8, Table 6). For the pseudo-first-order model, the R^2 values were consistently lower for all samples, with Si ($R^2 = 0.70422$), Ti ($R^2 = 0.54709$), and STiM

(R^2 = 0.28636). The relatively small difference in experimental and calculated q_e values for the Ti and STiM samples indicated that the pseudo-second-order model was more representative in describing the adsorption mechanism in these materials. The study of Hadian *et al.* [53] confirmed that the higher R^2 values for the pseudo-second-order model (>0.99) and the closeness between the experimental and calculated q_e values indicate that the adsorption follows a chemisorption mechanism. Revellame *et al.* [54] showed that the pseudo-second-order model consistently provided better fitting for the adsorption system of various pollutants, where the R^2 value > 0.98 indicated the validity of the model.

Table 6. Kinetic Models of all sample

Sample	C_o (ppm)	q_e Exp (mg/g)	Removal Efficiency (%)	Pseudo First Order			Pseudo Second Order		
				q_e Cal (mg/g)	K_1 (min^{-1})	R^2	q_e Cal (mg/g)	K_2 ($g.mg^{-1}\cdot min^{-1}$)	R^2
Si	10	0.000197	7.381	0.00693	−0.84402	0.70422	7.83964E-5	0.00222	0.65961
Ti	10	0.000597	27.381	0.02202	−0.67023	0.54709	4.66509E-4	0.00148	0.86629
STiM	10	0.001845	77.381	0.02146	0.45394	0.28636	0.00433	0.0084	0.82158

The adsorption rate constant analysis showed an interesting variation where the STiM sample had the highest pseudo-first-order rate constant (K_1) (0.45394 min^{-1}) with a positive value, in contrast to the Si and Ti samples which showed negative values. For the pseudo-second-order model, the STIM sample showed the highest rate constant (K_2) (0.0084 $g\cdot mg^{-1}\cdot min^{-1}$), followed by Ti (0.00148 $g\cdot mg^{-1}\cdot min^{-1}$) and Si (0.00222 $g\cdot mg^{-1}\cdot min^{-1}$). Kusworo [55] confirmed that the dominant pseudo-second-order model indicated a chemisorption mechanism as the rate-determining step with high affinity to the adsorbate. Banivaheb *et al.* [56] showed that a high rate constant correlates with superior adsorption capacity, where the composite material exhibits a higher rate constant than the single components. The high rate constant value in STiM indicates that the composite structure not only increases the adsorption capacity but also accelerates the adsorption kinetics through the formation of more diverse and accessible active sites. The dominance of the pseudo-second-order model indicates that the adsorption process involves the formation of chemical bonds between the adsorbate and active sites on the adsorbent surface, with the chemisorption mechanism as the rate-determining step in the removal process. The pseudo-second-order model is used here to describe the adsorption-influenced stage preceding photocatalytic degradation rather than the photon-driven reaction itself. In this study, the pseudo-second-order kinetic model is employed to describe the adsorption-controlled stage preceding photocatalytic degradation, rather than the photon-induced reaction mechanism itself. The pseudo-second-order kinetic model applied in this work reflects adsorption-dominated behavior and does not fully represent the mechanistic complexity of heterogeneous photocatalytic reactions.

The photocatalytic kinetics were analysed using the Langmuir–Hinshelwood framework under dilute concentration conditions, where the reaction rate can be reasonably approximated by a pseudo-first-order model (Fig 9). The linear fitting of $\ln(C_0/C_t)$ versus irradiation time provided apparent rate constants, enabling a reliable comparative evaluation of the photocatalytic activities of the investigated materials. Recycling and regeneration tests were not conducted in this study due to limitations in catalyst availability and experimental scope. Therefore, the long-term structural and catalytic stability of the materials could not be evaluated at this stage.

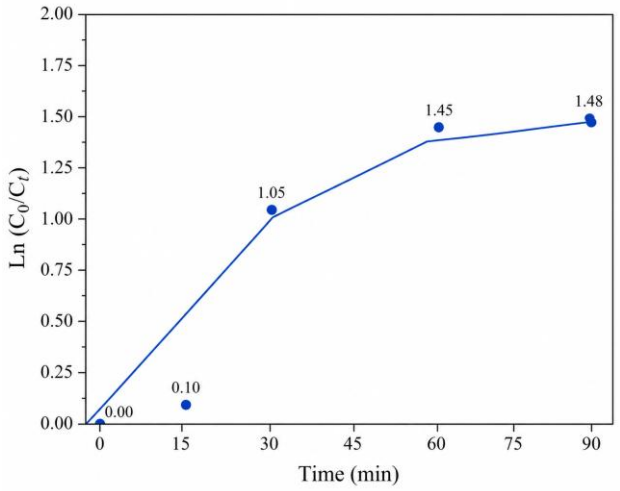

Fig. 9. Langmuir–Hinshelwood-based pseudo-first-order kinetic analysis under dilute MB conditions.

V. Conclusion

The comprehensive characterization of Si, Ti, and STiM nanocomposites demonstrates that structural integration and Mn doping induce profound modifications in crystallinity, morphology, surface area, and optical properties. The XRD and FTIR analyses confirmed the successful formation of heterogeneous bonding environments, while SEM-EDX evidenced morphological refinement and homogeneous elemental dispersion. BET and UV-DRS results revealed that the hierarchical micro–mesoporous structure and narrowed bandgap of STiM effectively enhanced visible-light utilization. Photocatalytic degradation experiments further established the superior efficiency of STiM (77.4%) over pristine Si and Ti, with kinetic modeling confirming the predominance of chemisorption pathways described by the pseudo-second-order model. These findings substantiate that the synergistic interplay between Si–Ti frameworks and Mn dopants is decisive in promoting charge separation, suppressing recombination, and facilitating catalytic reactivity. Overall, the study not only elucidates the structure–function relationships governing photocatalytic performance but also provides a robust foundation for designing next-generation nanocomposites tailored for large-scale environmental remediation applications.

Conflict of Interest

The authors declare no conflict of interest.

AUTHOR CONTRIBUTIONS

M. Ulfa: Conceptualization, Investigation, Methodology, Formal Analysis, Resources, Data Curation, Writing—Original Draft, Writing—Review & Editing, Supervision, Validation, Writing—Review & Editing, Data Curation A. Ardhany: Methodology, Formal Analysis, Data Curation, Project Administration. All authors have read and agreed to the published version of the manuscript.

FUNDING

This research is funded by the Indonesian Endowment Fund for Education (LPDP) on behalf of the Indonesian Ministry of Higher Education, Science and Technology and managed under the EQUITY Program of Universitas Sebelas Maret (Contract No. 4315/B3/DT.03.08/2025 and No. 84/UN27/KS/2025) in the scheme of Hibah International Research Network Program EQUITY THE Impact Rangkings 2025.

REFERENCES

[1] S. Dutta, S. Adhikary, S. Bhattacharya, D. Roy, S. Chatterjee, A. Chakraborty, D. Banerjee, A. Ganguly, S. Nanda, and P. Rajak, "Contamination of textile dyes in aquatic environment: Adverse impacts on aquatic ecosystem and human health, and its management using bioremediation," *Journal of Environmental Management*, vol. 353, Jan. 2024. doi: 10.1016/j.jenvman.2024.120103

[2] R. Al-Tohamy, S. S. Ali, F. Li, K. M. Okasha, Y. A. G. Mahmoud, T. Elsamahy, H. Jiao, Y. Fu, and J. Sun, "A critical review on the treatment of dye-containing wastewater: Ecotoxicological and health concerns of textile dyes and possible remediation approaches for environmental safety," *Ecotoxicology and Environmental Safety*, vol. 231, 2022. doi: 10.1016/j.ecoenv.2021.113160

[3] C. Amor, L. Marchão, M. S. Lucas, and J. A. Peres, "Application of advanced oxidation processes for the treatment of recalcitrant agro-industrial wastewater: A review," *Water (Switzerland)*, vol. 11, no. 2, 2019. doi: 10.3390/w11020205

[4] M. Asheghmoalla and M. Mehrvar, "Integrated and hybrid processes for the treatment of actual wastewaters containing micropollutants: A review on recent advances," *Processes*, vol. 12, no. 2, 2024. doi: 10.3390/pr12020339

[5] M. El Mchaouri, S. Mallah, D. Abouhajjoub, W. Boumya, R. Elmoubarki, A. Essadki, N. Barka, and A. Elhalil, "Engineering TiO_2 photocatalysts for enhanced visible-light activity in wastewater treatment applications," *Tetrahedron Green Chem*, vol. 6, Jul. 2025. doi: 10.1016/j.tgchem.2025.100084

[6] S. M. Fernandes, B. T. Barrocas, J. V. Nardeli, M. F. Montemor, E. Maçoas, M. C. Oliveira, C. C. C. R. de Carvalho, A. Lauria, M. Niederberger, and A. C. Marques, "Maximizing photocatalytic efficiency with minimal amount of gold: Solar-driven TiO_2 photocatalysis supported by MICROSCAFS® for facile catalyst recovery," *Journal of Environmental Chemical Engineering*, vol. 12, no. 2, 2024. doi: 10.1016/j.jece.2024.112043

[7] Y. Gong, Y. Wu, J. Shen, S. Zhao, X. Xu, J. Kang, L. Shen, Y. Zhou, Y. Zhao, and Z. Chen, "Generation of interfacial high-spin manganese intermediates as reactive oxidant during peroxymonosulfate activation mediated by amorphous MnOx supported on polymeric substrate," *Applied Catalysis B: Environmental*, vol. 316, Jun. 2022. doi: 10.1016/j.apcatb.2022.121671

[8] P. Cheng, Y. Li, Y. Ma, C. Qiu, T. Fu, Y. Wang, and F. Wu, "Amorphous Fe-doped manganese carbonate for efficient activation of peroxymonosulfate: Mechanism and performance toward orange II degradation," *Molecules*, vol. 30, no. 11, pp. 1–14, 2025. doi: 10.3390/molecules30112325

[9] X. L. Song, L. Chen, L. J. Gao, J. T. Ren, and Z. Y. Yuan, "Engineering g-C_3N_4 based materials for advanced photocatalysis: Recent advances," *Green Energy and Environment*, vol. 9, no. 2, pp. 166–197, 2024. doi: 10.1016/j.gee.2022.12.005

[10] D. Zhang, H. Cai, Y. Su, W. Sun, D. Yang, and G. A. Ozin, "Silica samurai: Aristocrat of energy and environmental catalysis," *Chem Catalysis*, vol. 2, no. 8, pp. 1893–1918, 2022. doi: 10.1016/j.checat.2022.06.001

[11] A. Pal, T. K. Jana, and K. Chatterjee, "Silica supported TiO_2 nanostructures for highly efficient photocatalytic application under visible light irradiation," *Materials Research Bulletin*, vol. 76, pp. 353–357, 2016. doi: 10.1016/j.materresbull.2015.12.040

[12] V. K. Yadav and M. H. Fulekar, "Green synthesis and characterization of amorphous silica nanoparticles from fly ash," *Materials Today: Proceedings*, vol. 18, pp. 4351–4359, 2019. doi: 10.1016/j.matpr.2019.07.395

[13] B. V. Dimas, I. H. Pérez, V. G. Febles, L. D. B. Arceo, R. S. Parra, J. N. R. Olvera, R. L. Paz, D. V. M. Máximo, and L. G. Reyes, "Atomic-scale investigation on the evolution of TiO_2-anatase prepared by a sonochemical route and treated with NaOH," *Materials*, vol. 13, no. 3, 2020. doi: 10.3390/ma13030685

[14] V. L. Chandraboss, "Sol-gel synthesis and photocatalytic application of MnO_2@SiO_2 composite material," *Malaya Journal of Matematik*, vol. S, no. 2, pp. 2191–2193, 2020.

[15] S. H. Siregar, P. Prasetya, N. Norramizawati, M. Marlian, and A. R. Ramadhanti, "Titanium dioxide (TiO_2) modified bentonite for photodegradation in methylene blue dye," *Jurnal Kimia Sains dan Aplikasi*, vol. 26, no. 4, pp. 143–150, 2023. doi: 10.14710/jksa.26.4.143-150

[16] P. E. Imoisili, K. O. Ukoba, and T. C. Jen, "Synthesis and characterization of amorphous mesoporous silica from palm kernel shell ash," *Boletin de la Sociedad Espanola de Ceramica y Vidrio*, vol. 59, no. 4, pp. 159–164, 2020. doi: 10.1016/j.bsecv.2019.09.006

[17] S. Fany Mulya Putri, T. Dwi Restika, and R. Jonuarti, "Effect of calcination temperature of SiO_2-TiO_2 composite XRD characterization of crystal size structure and phase," *Journal of Experimental and Applied Physics*, vol. 2, no. 3, 16, 2024.

[18] C. A. Duarte, L. R. Goulart, letícia de S. C. Filice *et al*., "Characterization of crystalline phase of TiO_2," *Materials*, vol. 13, 4071, 2020.

[19] M. G. Kim, J. M. Kang, J. E. Lee, K. S. Kim, K. H. Kim, M. Cho, and S. G. Lee, "Effects of calcination temperature on the phase composition, photocatalytic degradation, and virucidal activities of TiO_2 nanoparticles," *ACS Omega*, vol. 6, no. 16, pp. 10668–10678, 2021. doi: 10.1021/acsomega.1c00043

[20] S. Nasiri, M. Rabiei, A. Palevicius, G. Janusas, A. Vilkauskas, V. Nutalapati, and A. Monshi, "Modified Scherrer equation to calculate crystal size by XRD with high accuracy, examples Fe_2O_3, TiO_2 and V_2O_5," *Nano Trends*, vol. 3, Aug. 2023. doi: 10.1016/j.nwnano.2023.100015

[21] M. M. Ilmi, N. Nurdini, E. Maryanti, P. Setiawan, and I. Ismunandar, "X-ray diffraction peak profile for determination of microstructural properties of hematite (Fe_2O_3)," *Journal of Research and Development on Nanotechnology*, vol. 1, no. 1, pp. 11–17, 2021. doi: 10.5614/jrdn.2021.1.1.16667

[22] A. Teamsinsungvon, C. Ruksakulpiwat, P. Amonpattaratkit, and Y. Ruksakulpiwat, "Structural characterization of titanium–silica oxide using synchrotron radiation X-ray absorption spectroscopy," *Polymers*, vol. 14, no. 13, pp. 1–27, 2022. doi: 10.3390/polym14132729

[23] R. Nandanwar, J. Bamne, N. Singh, K. Taiwade, V. Chandel, P. K. Sharma, P. Singh, A. Umar, and F. Z. Haque, "Synthesis of titania-silica nanocomposite for enhanced photodegradation of methylene blue and methyl orange dyes under UV and mercury lights," *ES Materials and Manufacturing*, vol. 16, pp. 78–88, 2022. doi: 10.30919/esmm5f628

[24] A. H. Diputra, I. K. Hariscandra Dinatha, and Y. Yusuf, "A comparative X-ray diffraction analysis of Sr^{2+} substituted hydroxyapatite from sand lobster shell waste using various methods," *Heliyon*, vol. 11, no. 2, 2025. doi: 10.1016/j.heliyon.2025.e41781

[25] M. T. Ulhakim, S. Sukarman, K. Khoirudin, N. Fazrin, T. Irfani, and A. Hakim, "Determining the crystallite size of TiO_2/EG-Water XRD data using the Scherrer equation," *Indonesian Journal of Applied Physics*, vol. 14, no. 1, 141, 2024. doi: 10.13057/ijap.v14i1.79195

[26] R. Ellerbrock, M. Stein, and J. Schaller, "Comparing amorphous silica, short-range-ordered silicates and silicic acid species by FTIR," *Scientific Reports*, vol. 12, no. 1, pp. 1–8, 2022. doi: 10.1038/s41598-022-15882-4

[27] R. H. Ellerbrock, M. Stein, and J. Schaller, "Comparing silicon mineral species of different crystallinity using Fourier transform infrared spectroscopy," *Frontiers in Environmental Chemistry*, vol. 5, pp. 1–9, Oct. 2024. doi: 10.3389/fenvc.2024.1462678

[28] P. S. Ramaripa, K. D. Modibane, K. Makgopa, O. A. Seerane, M. S. Maubane-Nkadimeng, E. Makhado, M. J. Hato, M. E. Ramoroka, K. M. Molapo, D. Balakrishnan, and E. I. Iwuoha, "Fabrication, characterization, and photovoltaic performance of titanium dioxide/metal-organic framework composite," *Journal of Photochemistry and Photobiology*, vol. 12, Aug. 2022. doi: 10.1016/j.jpap.2022.100142

[29] L. Jothi and P. Divya, "Synthesis and characterization of MnO_2 nanoparticles prepared by hydrothermal processing," *International Journal of Science, Engineering and Technology*, vol. 7, no. 6, 6, 2019.
[30] T. Noguchi, "FTIR detection of water reactions in the oxygen-evolving centre of photosystem II," *Philosophical Transactions of the Royal Society B: Biological Sciences*, vol. 363, no. 1494, pp. 1189–1195, 2008. doi: 10.1098/rstb.2007.2214
[31] F. Dai, Q. Zhuang, G. Huang, H. Deng, and X. Zhang, "Infrared spectrum characteristics and quantification of OH groups in coal," *ACS Omega*, vol. 8, no. 19, pp. 17064–17076, 2023. doi: 10.1021/acsomega.3c01336
[32] S. A. Mousa, H. Abdallah, and S. A. Khairy, "The use of green synthesized TiO_2/MnO_2 nanoparticles in solar power membranes for pulp and paper industry wastewater treatment," *Scientific Reports*, vol. 15, no. 1, pp. 1–21, 2025. doi: 10.1038/s41598-024-85075-8
[33] H. A. Budiarti, R. N. Puspitasari, A. M. Hatta, R. Sekartedjo, and D. D. Risanti, "Synthesis and characterization of TiO_2@SiO_2 and SiO_2@TiO_2 core-shell structure using Lapindo mud extract via sol-gel method," *Procedia Engineering*, vol. 170, pp. 65–71, 2017. doi: 10.1016/j.proeng.2017.03.013
[34] X. Wei, Y. Lu, X. Liu, B. Zhang, M. Luo, and L. Zhong, "Particle shape analysis of calcareous sand based on digital images," *Scientific Reports*, vol. 14, no. 1, pp. 1–14, 2024. doi: 10.1038/s41598-024-69197-7
[35] J. Bals and M. Epple, "Deep learning for automated size and shape analysis of nanoparticles in scanning electron microscopy," *RSC Advances*, vol. 13, no. 5, pp. 2795–2802, 2023. doi: 10.1039/d2ra07812k
[36] F. Dong, C. Liu, Y. Zhang, X. Yuan, B. Wang, L. Luo, Y. Su, J. Cheng, Y. Tian, and P. K. Liaw, "Preparation and characterization of a dual-structure-embedded, reinforced titanium matrix composite powder using an ultrasonic atomization method," *Journal of Alloys and Compounds*, vol. 1035, Jun. 2025. doi: 10.1016/j.jallcom.2025.181558
[37] S. Sankaranarayanan, B. Likozar, and R. Navia, "Real-time particle size analysis using the focused beam reflectance measurement probe for in situ fabrication of polyacrylamide–filler composite materials," *Scientific Reports*, vol. 9, no. 1, pp. 1–12, 2019. doi: 10.1038/s41598-019-46451-x
[38] J. E. Karbowniczek, D. P. Ura, and U. Stachewicz, "Nanoparticles distribution and agglomeration analysis in electrospun fiber based composites for desired mechanical performance of poly(3-hydroxybutyrate-co-3-hydroxyvalerate (PHBV) scaffolds with hydroxyapatite (HA) and titanium dioxide (TiO_2) towards me," *Composites Part B: Engineering*, vol. 241, Mar. 2022. doi: 10.1016/j.compositesb.2022.110011
[39] L. Wang, G. Xie, X. Mi, B. Zhang, Y. Du, Q. Zhu, and Z. Yu, "Surface-modified TiO_2@SiO_2 nanocomposites for enhanced dispersibility and optical performance to apply in the printing process as a pigment," *ACS Omega*, vol. 8, no. 22, pp. 20116–20124, 2023. doi: 10.1021/acsomega.3c02679
[40] L. Kadri, A. Abderrahmane, G. Bulai, A. Carlescu, C. Doroftei, I. Motrescu, S. Gurlui, L. Leontie, and M. Adnane, "Optical and structural analysis of TiO_2–SiO_2 nanocomposite thin films fabricated via pulsed laser deposition technique," *Nanomaterials*, vol. 13, no. 10, 2023. doi: 10.3390/nano13101632
[41] B. T. da Fonseca, E. D'Elia, J. M. Siqueira Júnior, S. M. de Oliveira, K. L. dos Santos Castro, and E. S. Ribeiro, "Study of the characteristics and properties of the SiO_2/TiO_2/Nb_2O_5 material obtained by the sol–gel process," *Scientific Reports*, vol. 11, no. 1, pp. 1–15, 2021. doi: 10.1038/s41598-020-80310-4
[42] J. Choma, J. Jagiello, and M. Jaroniec, "Assessing the contribution of micropores and mesopores from nitrogen adsorption on nanoporous carbons: Application to pore size analysis," *Carbon*, vol. 183, pp. 150–157, 2021. doi: 10.1016/j.carbon.2021.07.020
[43] L. A. J. Garvie, L. Trif, D. Cotto-Figueroa, E. Asphaug, and C. G. Hoover, "High surface area and interconnected nanoporosity of clay-rich astromaterials," *Scientific Reports*, vol. 14, no. 1, pp. 1–11, 2024. doi: 10.1038/s41598-024-61114-2
[44] M. Bonne, S. Pronier, F. Can, X. Courtois, S. Valange, J. M. Tatibouët, S. Royer, P. Marécot, and D. Duprez, "Synthesis and characterization of high surface area TiO_2/SiO_2 mesostructured nanocomposite," *Solid State Sciences*, vol. 12, no. 6, pp. 1002–1012, 2010. doi: 10.1016/j.solidstatesciences.2009.10.009
[45] N. Xiao, A. Zhang, K. Yuan, and W. Cao, "Robust mesoporous SiO_2-coated TiO_2 colloidal nanocrystal with enhanced adsorption, stability, and adhesion for photocatalytic antibacterial and benzene removal," *Materials*, vol. 18, no. 16, pp. 1–14, 2025. doi: 10.3390/ma18163844
[46] P. Makuła, M. Pacia, and W. Macyk, "How to correctly determine the band gap energy of modified semiconductor photocatalysts based on UV-Vis spectra," *Journal of Physical Chemistry Letters*, vol. 9, no. 23, pp. 6814–6817, 2018. doi: 10.1021/acs.jpclett.8b02892
[47] S. Landi, I. R. Segundo, C. Afonso, O. Lima, M. F. M. Costa, E. Freitas, and J. Carneiro, "Evaluation of band gap energy of TiO_2 precipitated from titanium sulphate," *Physica B: Condensed Matter*, vol. 639, pp. 10–13, May 2022. doi: 10.1016/j.physb.2022.414008
[48] S. Halder, R. A. Kumar, R. Maity, and T. P. Sinha, "A tailored direct-to-indirect band structure transition in double perovskite oxides influences its photocatalysis efficiency," *Ceramics International*, vol. 49, no. 5, pp. 8634–8645, 2023. doi: 10.1016/j.ceramint.2022.12.096
[49] P. L. Hariani, S. Salni, M. Said, and R. Farahdiba, "Core-shell Fe_3O_4/SiO_2/TiO_2 magnetic modified Ag for the photocatalytic degradation of Congo red dye and antibacterial activity," *Bulletin of Chemical Reaction Engineering and Catalysis*, vol. 18, no. 2, pp. 315–330, 2023. doi: 10.9767/bcrec.19275
[50] Y. Etafa Tasisa, T. Kumar Sarma, R. Krishnaraj, and S. Sarma, "Band gap engineering of titanium dioxide (TiO_2) nanoparticles prepared via green route and its visible light driven for environmental remediation," *Results in Chemistry*, vol. 11, Aug. 2024. doi: 10.1016/j.rechem.2024.101850
[51] A. Doyan, S. Susilawati, and L. Muliyadi, "Analysis of the energy band gap of tin oxide thin layers as semiconductor base materials in electronic devices," *Jurnal Penelitian Pendidikan IPA*, vol. 8, no. 6, pp. 2772–2777, 2022. doi: 10.29303/jppipa.v8i6.2657
[52] S. Khaliha, D. Jones, A. Kovtun, M. L. Navacchia, M. Zambianchi, M. Melucci, and V. Palermo, "The removal efficiency of emerging organic contaminants, heavy metals and dyes: Intrinsic limits at low concentrations," *Environmental Science: Water Research and Technology*, vol. 9, no. 6, pp. 1558–1565, 2023. doi: 10.1039/d2ew00644h
[53] D. Hadian, A. Alni, A. Patah, N. Handayani, and M. A. L. I. Zulfikar, "Efficient removal of Pb(II) ion using TiO_2/ZnO/SiO_2 nanocomposite from aqueous solutions via adsorption-photocatalysis process," *Sains Malaysiana*, vol. 53, no. 5, pp. 1133–1147, 2024. doi: 10.17576/jsm-2024-5305-13
[54] E. D. Revellame, D. L. Fortela, W. Sharp, R. Hernandez, and M. E. Zappi, "Adsorption kinetic modeling using pseudo-first order and pseudo-second order rate laws: A review," *Cleaner Engineering and Technology*, vol. 1, Dec. 2020. doi: 10.1016/j.clet.2020.100032
[55] T. D. Kusworo, "Kinetic and isotherm analysis of TiO_2/UiO-66-NH_2 composites for treating produced water contaminants," *Waste Tech.*, vol. 12, pp. 60–66, Oct. 2024.
[56] S. Banivaheb, S. Dan, H. Hashemipour, and M. Kalantari, "Synthesis of modified chitosan TiO_2 and SiO_2 hydrogel nanocomposites for cadmium removal," *Journal of Saudi Chemical Society*, vol. 25, no. 8, 2021. doi: 10.1016/j.jscs.2021.101283